Proton substructure and conductivity in the room-temperature proton conductors $Zr_{1-x}Sc_xH_{5+x}(PO_4)_3$

Lara M. Gronych[a], Jędrzej Kondek[a,b,c], Marvin A. Kraft[a,d], Xabier Martinez de Irujo Labalde[a], Dana Glikman[b], Jon A. Newnham[a,e], Cheng Li[f], Vasiliki Faka[a], Daria S. Stepaniuk[g-k],, Volodymyr Baran[l], Björn Braunschweig[c], Doreen Mollenhauer[g-k], Michael Ryan Hansen[c] and Wolfgang G. Zeier*[a,b]

[a]*Institute of Inorganic and Analytical Chemistry, University of Münster, Corrensstrasse 28/30, 48149 Münster, Germany.*

[b]*Institut für Physikalische Chemie, Universität Münster, Corrensstrasse 30, 48149 Münster, Germany.*

[c]*International Graduate School for Battery Chemistry, Characterization, Analysis, Recycling and Application (BACCARA), University of Münster, 48149 Münster, Germany.*

[d]*Institute of Energy Materials and Devices (IMD), IMD-4: Helmholtz-Institut Münster, Forschungszentrum Jülich, 48149 Münster, Germany.*

[e]*Advanced Centre for Energy and Sustainability, Department of Chemistry, School of Natural and Computing Sciences, University of Aberdeen, Aberdeen AB24 3FX, U.K.*

[f]*Neutron Scattering Division, Oak Ridge National Laboratory, Oak Ridge, TN 37830, USA.*

[g]*Institute of Physical Chemistry, Justus Liebig University Gießen, Heinrich-Buff-Ring 17, 35392 Gießen, Germany.*

[h]*Center for Materials Research, Justus Liebig University Gießen, Heinrich-Buff-Ring 16, 35392 Gießen, Germany.*

[i]*Institute for Technical and Environmental Chemistry, Friedrich Schiller University Jena, Philosophenweg 7a, 07743 Jena, Germany.*

[j]*Helmholtz Institute for Polymers in Energy Applications Jena (HIPOLE Jena), Lessingstrasse 12-14, 07743 Jena, Germany.*

[k]*Helmholtz-Zentrum Berlin für Materialien und Energie GmbH (HZB), Hahn-Meitner-Platz 1, 14109 Berlin, Germany.*

[l]*Deutsches Elektronen-Synchrotron DESY, Notkestrasse. 85, 22607 Hamburg, Germany.*

*wzeier@uni-muenster.de

Abstract

Solid proton conductors are an important materials class when it comes to the further development of hydrogen-based devices for energy generation and storage. These applications make it essential to get high proton conductivity and stability at around 25 °C without the need for additional humidification. The proton conductor zirconium acid triphosphate ($ZrH_5(PO_4)_3$) has been shown to meet these requirements and is therefore of interest. In this work, we present a systematic study of Sc-substituted $Zr_{1-x}Sc_xH_{5+x}(PO_4)_3$ samples in the range of $0 \leq x \leq 1$. The structure and proton transport properties are investigated by neutron powder and X-ray diffraction data, second-harmonic generation measurements, nuclear magnetic resonance and impedance spectroscopy. The obtained results provide a better understanding of the H^+ network in $ZrH_5(PO_4)_3$, implying a disordered arrangement. This is not observed in $ScH_6(PO_4)_3$, which, in contrast to $ZrH_5(PO_4)_3$ with 1.7(4) mS cm^{-1} at 25 °C, has a significantly lower proton conductivity of 3.1(6) $\cdot 10^{-4}$ mS cm^{-1}. The aim of this work is to give deeper insight into the structure-property relationship of this class of proton conductors to contribute to the further development of materials.

Keywords

Solid Proton Electrolyte

Anhydrous Proton Conductor

Aliovalent/Partial Substitution

(Zirconium-)Hydrogen phosphate

Structural Analysis

Full structural solution

1. Introduction

Solid proton conductors are important for various applications including fuel cells, sensors and electrolyzers.[1] The requirements for such devices are constantly diversifying, with the application of hydrogen-based technologies at the forefront.[2,3] It is important to develop even more efficient ways for electricity generation and energy storage, making the investigation and improvement of electrochemical devices such as fuel cells or electrolyzers important.[4] For instance, proton conductivity influences and determines the characteristics of these devices, while high proton conductivity together with good chemical and thermal stability are a necessity.[5,6]

For solid-state proton conductors, several different materials exist that can be categorized, according to their chemical composition, structure or preparation method.[7] Examples are Nafion,®[8–10] metal-organic frameworks[11,12], as well as various oxides and solid acids.[13] The organic polymer Nafion® is a commercial material for fuel cells achieving conductivities of up to 10^{-1} S cm^{-1} in a temperature range of 50 °C – 100 °C in its hydrated form.[8–10] However, the material also has the challenge of a significant drop in conductivity at high temperatures, and sufficient hydration of the polymer must be ensured.[9] Within metal-organic frameworks, proton conductivities of 10^{-2} – 10^{-1} S cm^{-1} at temperatures around 85 °C are possible, but highly humidified atmospheres with a relative humidity up to 99% are required.[11,12]

Beyond the previous materials, oxides comprise a large group of proton conductors, including perovskite-, brownmillerite- and pyrochlore-type compounds.[14–16] Since the discovery of proton conductivity in $SrCeO_3$ by Iwahara *et al.*[17] in the 1980s, perovskites are of interest for use as proton conductors. The most studied compounds are doped barium cerate and zirconate-based perovskites which show high proton conductivities, as well as sufficient chemical stability.[16,18] The advantage of oxides is their high thermal stability and proton conductivity at temperatures above 600 °C, but the drop in proton conductivity at moderate temperatures remains a drawback.[7,16] Solid acids with the general composition $MHAO_4$ or $M_3H(AO_4)_2$ (M = alkali metal or NH_4; A = S, Se) or similar variations, for example, can be used for proton conduction in the temperature range of 120 °C – 300 °C.[19,20] While these materials have low conductivity at room temperature, they undergo a temperature driven superprotonic phase transition.[19,20] This leads to a disordered H^+ bond network, resulting in a significant increase in conductivity.[21] The main drawbacks of this type of proton conductor are the need of the high humidity and temperature to stabilize the superprotonic phase. Otherwise, the material will decompose and lose protons/water.[19] The fact that the solid acids only show sufficient proton conductivity within a specific temperature range limits the applicational use. For example, one

of the most studied solid acids, $CsHSO_4$, undergoes a superprotonic phase transformation at 141 °C. From 200 °C – 230 °C, $CsHSO_4$ starts to decompose, resulting in a relatively narrow temperature window for applications.[22] However, phosphate-based derivatives are also found among the solid acids, such as CsH_2PO_4.[23] This compound exhibits a superprotonic phase transition at (228 ± 2) °C.[23] It was found that the increase in conductivity depends heavily on the sample, and that this phase transition competes with the thermal decomposition of the material under atmospheric pressure.[23] Increasing the pressure can prevent this decomposition.[23] Another phosphate-based proton conductor is In^{3+}-doped SnP_2O_7, for example. In its undoped form, its proton conductivity is $5.56 \cdot 10^{-2}$ S cm^{-1} at 250 °C.[24] Aliovalent substitution of Sn^{4+} with In^{3+} causes an increase in the proton concentration in the bulk, thus enhancing the proton conductivity to $1.95 \cdot 10^{-1}$ S cm^{-1}.[24]

The high relative humidity often required for proton conduction and the relatively high temperatures represents a key challenge among the different classes of solid proton conductors in the development and application of new materials. The number of proton conductors exhibiting a high proton conductivity at temperatures below 100 °C and not require humidification is limited. Therefore, the conductivity of 10^{-3} S cm^{-1} even at room temperature under anhydrous conditions is what makes the recently reported proton conductor zirconium acid triphosphate ($ZrH_5(PO_4)_3$) of such interest for various energy applications like proton batteries and proton exchange membrane fuel cells.[13,25,26] The latter requires a proton conductor with high conductivity in a temperature range of 80 °C – 120 °C and, ideally, low humidity. Accordingly, $ZrH_5(PO_4)_3$ would be well-suited to this purpose.[26] Fop *et al*. investigated the underlying mechanism and revealed that the fast proton conduction is enabled by H^+ channels through the structure, suggesting a Grotthus-like mechanism.[13] Since $ZrH_5(PO_4)_3$ already contains protons in its structure, the underlying mechanism of proton conductivity differs from that of materials that require high humidity for conduction. In In^{3+}-doped SnP_2O_7, for example, the protons must first be formed in the bulk using water and electron holes.[24] Moreover, materials that are structurally related to $ZrH_5(PO_4)_3$ are known in the literature,[27,28] but their proton conductivity has not yet been investigated. Based on these previous studies, this work focuses on gaining further insight into the structure-property relationship of the $ZrH_5(PO_4)_3$-type proton conductors. Therefore, the proton conductors $Zr_{1-x}Sc_xH_{5+x}(PO_4)_3$ ($0 \leq x \leq 1$) were synthesized and the proton positions in the structures of $ZrH_5(PO_4)_3$ and $ScH_6(PO_4)_3$ determined using neutron diffraction. Furthermore, the ionic conductivity upon aliovalent substitution is monitored and decreases in a vacancy filling fashion in line with significantly increased

activation energies. Overall, this work provides a deep investigation into the structure – property relationship of this interesting class of room-temperature proton conductors.

2. Experimental Section

***Synthesis*.** Compounds according to the targeted nominal stoichiometry $Zr_{1-x}Sc_xH_{5+x}(PO_4)_3$ ($0 \leq x_{nom} \leq 1$; in 0.25 steps) were synthesized via precipitation reactions. The anhydrous precursors $ZrCl_4$ (*Merck*, 99.9%) and $ScCl_3$ (*Sigma Aldrich*, 99.9%, trace metal basis) and H_3PO_4 (*Sigma Aldrich*, ≥99.999%, trace metal basis) were stored and weighed under dry Ar atmosphere. The metal chlorides were weighed stoichiometrically and ground together in a mortar. The phosphoric acid was weighed in with excess, according to a molar ratio *M*:P (*M* = Zr and/or Sc) of 1:25.[31] The phosphoric acid was heated to melt at 85 °C in an open vessel and the metal chlorides were added. For $ZrH_5(PO_4)_3$, a white solid precipitated after a few minutes. In the case of $ScH_6(PO_4)_3$, precipitation occurred only after a few hours. In total, the mixture was stirred for 48 h at 85 °C. After that, the precipitate was isolated by centrifugating and washing five times with acetone (*Acros Organics*, ≥99.8%). Finally, the solids were filtered and dried at 90 °C under dynamic vacuum to remove any residues of acetone. The resulting powders were hand-ground and stored under dry Ar atmosphere to prevent decomposition at room atmosphere. In accordance with the thermal analysis of $ZrH_5(PO_4)_3$ by Fop *et al.*,[13] in this study, the decomposition of $ZrH_5(PO_4)_3$ after exposition to air was observed. However, $ScH_6(PO_4)_3$ was stable under atmospheric conditions.

X-ray powder diffraction for Rietveld analysis. X-ray powder diffraction data of $Zr_{1-x}Sc_xH_{5+x}(PO_4)_3$ ($0 \leq x_{nom} \leq 1$) were collected using a STOE STADI P diffractometer with Mo $K\alpha_1$ radiation (λ = 0.70930 Å) and a Ge(111) monochromator (Stoe & Cie GmbH). The diffractograms were recorded with a Dectris MYTHEN2 2K detector in Debye-Scherrer geometry. The measurements were carried out on the powder samples in spinning sealed glass borosilicate capillaries ($\varnothing_{inner}$ = 0.5 mm) within a *Q*-range of 0.1 $Å^{-1}$ to 8 $Å^{-1}$. The capillaries were prepared under Ar atmosphere.

Neutron powder diffraction (NPD). Neutron powder diffraction data of $ZrH_5(PO_4)_3$ and $ScH_6(PO_4)_3$ were collected at the Oak Ridge spallation neutron source (SNS, Oak Ridge National Laboratory) at the POWGEN diffractometer (BM11-A beamline) with the PAC automatic sample changer.[29] 6 mm diameter cylindrical vanadium cans were used to measure the samples. The cans were filled with approximately 1.5 g of sample and sealed with a copper

gasket under He atmosphere. The measurements were carried out with a center wavelength of 1.5 Å at three different temperatures (10 K, 100 K and 300 K) for 2 h collecting on a single bank.

Rietveld analysis. Rietveld refinements were performed utilizing the TOPAS-Academic V7.25 software package.[30] The fit indicators R_{wp} and goodness of fit (GOF) were used to verify the fit quality. Initially (1) background coefficients of a Chebyshev polynomial function, (2) the scale factor, (3) a full axial model for the peak asymmetry by axial divergence, (4) a zero-point offset, (5) the peak shape and (6) the lattice parameters were allowed to refine. After that, (7) the fractional atomic coordinates, (8) atomic displacement parameters as well as (9) occupancies of each atomic position were allowed to refine. The atomic displacement parameters of the $(PO_4)^{3-}$ unit are refined as rigid unit. The trigonal starting model ($R\bar{3}c$) tested for $ZrH_5(PO_4)_3$ was according Fop *et al.*[13] For $ScH_6(PO_4)_3$, the trigonal starting models ($R\bar{3}c$, $R3c$) were tested.[27,28] To search and test other possible space groups for $ZrH_5(PO_4)_3$, ISODISTORT was used,[31] producing the trigonal structural starting model for refinements. Based on the reported trigonal crystal structure, the ISODISPLACE integration allows to list equivalent structure models of lower symmetry including distortions upon further structure refinements. Tested space groups were $R\bar{3}c$, $R3c$, $R32$ and $R\bar{3}$.[31] The polyhedral volumes were extracted from the refined structures in VESTA, which was also used to create the structural representations shown.[32]

Potentiostatic electrochemical impedance spectroscopy (PEIS). The proton conductivities were determined using potentiostatic impedance spectroscopy. Approximately 200 mg of each sample was pressed into pellets with a diameter of 10 mm resulting in a thickness of 1.8 mm. The pellets were initially formed in a pressing die using a manual screw press and then isostatically pressed for 40 minutes at 435 MPa protected from the hydraulic fluid by evacuated silicone rubber sleeves. After that, Pt electrodes (8 mm diameter) were deposited on both sides of the pellet by DC magnetron sputtering (300 s, 30 mA, Cressington Sputter Coater 108auto). Afterwards, the platinum electrodes were contacted with aluminum current collectors and sealed into pouch foil under argon atmosphere. The impedance measurements were conducted with an Alpha-A impedance analyzer (Novocontrol Technologies GmbH) in the temperature range from 25 °C to 80 °C and within a frequency range of 10 MHz to 0.1 Hz of the sinusoidal excitation voltage of 14 mV amplitude. The impedance spectra were analyzed using the software RelaxIS 3 (rhd instruments).

Bond valence site energy (BVSE) calculations. The bond valence site energies for the migration of H^+ and their pathways were calculated using the program SoftBV V1.3.1. based on the refined structural models of the Bragg data.[33,34] The calculations were performed with a resolution of $(0.1\ Å)^3$ and a constant screening factor of 0.649 as the average automatically estimated value of all evaluated structures.

Second-harmonic generation (SHG). SHG signals were recorded using a Ti:sapphire oscillator (Spectra-Physics, MaiTai SP) operating with at a repetition rate of 80 MHz, a center wavelength of 800 nm, 10 nm bandwidth, and with ~90 fs pulse duration. SHG signals of four different polarization combinations (PP, SP, PS, SS) were recorded with each sample measured in triplicate. SHG photons were detected using a photon counting unit (Hamamatsu, C3866). Powder samples were placed in glass capillaries ($Ø_{inner}$ = 0.3 mm), and SHG measurements were conducted by varying the scattering angle from −110° to +90°, with results averaged over this range. Additional details on the SHG spectrometer used here can be found elsewhere.[35]

Computational details. All total energy calculations were performed using density functional theory (DFT) as implemented in the Vienna Ab-initio Simulation Package (VASP).[36–38] The exchange-correlation interactions were described using the Perdew-Burke-Ernzerhof (PBE) density functional within the generalized gradient approximation (GGA).[39] Van der Waals interactions were accounted for using Grimme's D3 dispersion[40] correction with Becke-Jonson damping[41]. The interactions between core and valence electrons were simulated using projector augmented wave potentials (PAW P).[42,43] The k-point test showed that the difference between 1x1x1 and 2x2x1 and higher meshes was only 0.2 eV, so the Gamma-point (1x1x1) mesh was used for all the calculations. The plane-wave cut-off energy was set to 500 eV, and the Brillouin zone sampling was restricted to the Γ-point due to the large supercell size (six formula units). The cut-off energy test was conducted by varying energies in the range 250 eV – 600 eV. Phonon calculations were performed using the finite displacement method as implemented in Phonopy.[44] The interatomic force constants were obtained from the supercell approach, using a 2×2×1 supercell with atomic displacements of 0.01 Å. The size of the supercell was increased to 24 formula units to avoid artificial interactions that could affect the forces and, consequently, the frequencies in the calculations. The phonon density of state (DOS) was computed by Fourier transforming the dynamical matrix and interpolating over a dense 20x20x20 q-point mesh. The vibrational entropy and thermodynamic properties were derived from the phonon free energy contributions at finite temperatures.

Nuclear magnetic resonance (NMR) spectroscopy. Hahn-echo ^{1}H and single-pulse ^{31}P MAS NMR experiments were performed using a Bruker AVANCE NEO 500 spectrometer equipped with a wide-bore superconducting magnet operating at 11.75 T ($\nu_0(^{1}H)$ = 500.13 MHz, $\nu_0(^{31}P)$ = 202.40 MHz) and a H/F-X MAS NMR probe (Bruker). Samples were packed into 2.5 mm outer diameter zirconia rotors under an Ar atmosphere. A MAS frequency of 25.0 kHz was used as well as radio-frequency (rf) pulse lengths of 3.5 µs (^{1}H) and 4.38 µs (^{31}P) corresponding to 90° flip angles. Recycle delays of 10 s (^{1}H) and 30 s (^{31}P) were used to ensure full relaxation. The MAS NMR spectra were referenced to solid adamantane (^{1}H, 1.85 ppm) and 1 M H_3PO_4 (^{31}P, 0.0 ppm) prior to all experiments. Static single-pulse ^{45}Sc NMR experiments were performed using a Bruker AVANCE III 300 spectrometer equipped with a wide-bore superconducting magnet operating at 7.05 T ($\nu_0(^{45}Sc)$ = 72.88 MHz) and a static 5.0 mm HX NMR probe (Bruker). Samples were packed into 4.0 mm outer diameter zirconia rotors under an Ar atmosphere. A rf pulse length of 0.97 µs was used for a central transition selective rf pulse corresponding to 22.5° flip angle. The ^{45}Sc NMR spectra were referenced to $ScCl_3$ (0.0 ppm). Static variable-temperature (VT) saturation-recovery ^{1}H NMR experiments were performed using a Bruker AVANCE NEO 200 spectrometer equipped with a wide-bore magnet operating at 4.70 T using a static 5.0 mm HX NMR probe (Bruker). All experiments were conducted at a Larmor frequency of 200.1 MHz using a rf pulse length of 4.5 µs for a 90° flip angle. The sample temperature was regulated by using a nitrogen gas flow and electrical heating. In the temperature range from 214 K to 295 K, an Air Jet XR compressor-based cooling system from SP Scientific (FTS Systems) was used. Static VT saturation-recovery ^{1}H NMR experiments were additionally measured on a Bruker Minispec (mq20) spectrometer operating at a 0.46 T. All experiments were conducted at a Larmor frequency of 19.95 MHz using a rf pulse length of 2.64 µs for 90° flip angle. The sample temperature was regulated by using a nitrogen gas flow and electrical heating. In the temperature range from 225 K to 300 K, an Air Jet XR compressor-based cooling system from SP Scientific (FTS Systems) was used. Activation energies (E_a) were obtained from saturation recovery data using the modified BPP model.[45] An extended description of data fitting routine is included in the Supporting Information.

3. Results and Discussion

Structure of $ZrH_5(PO_4)_3$. $ZrH_5(PO_4)_3$ was previously reported to crystallize in the $R\bar{3}c$ space group.[13] This structure was obtained based on refinements against powder X-ray diffraction data, and the proton positions were obtained by Bond Valence Sum Energy calculations. However, due to the light weight of the oxide anions, and the protons being virtually undetectable to X-rays, this structural solution may be able to be improved upon, and the H^+ conduction pathways may be still better-defined using neutron diffraction data (NPD). Therefore, to gain a better understanding of the proton substructure, $ZrH_5(PO_4)_3$ was synthesized according to the previously described method, and the neutron diffraction patterns of the material were collected at 10 K, 100 K and 300 K (Figure S1).

Using both neutron and X-ray diffraction data, Rietveld refinements were performed using the $R\bar{3}$c structure model according to Fop *et al.*[13] (Figure S1 and Figure S2). Against both data sets, refinements could be achieved with fit statistics within a reasonable range. However, the values of the atomic displacement parameters associated with the $(PO_4)^{3-}$ units and the protons seem high (Table S1 – S3) compared to values that would be expected from structurally related electrolytes.[46] In these refinements, the $(PO_4)^{3-}$ units were refined as a rigid unit mode with the atomic displacement parameters of both oxygen and phosphorus in the polyanions being constrained equal. Similarly, the displacement parameters associated with both proton positions were constrained equal. This refinement approach was used in both refinements against neutron and X-ray data. In these refinements, B_{eq} values of 5.7(3) Å^2 and 1.78(6) Å^2 were obtained for the protons and the $(PO_4)^{3-}$ rigid units at 10 K and 6.9(4) Å^2 and 2.39(4) Å^2 at 300 K, respectively. Especially at these low temperatures, such elevated values are suggesting static disorder in the structure. Indeed, Azad *et al*. observe comparably high B_{eq} values (6.4(6) Å^2 at 5 K and 8.5(6) Å^2 at 300 K) for deuterium in the $BaCe_{0.4}Zr_{0.4}Sc_{0.2}O_{2.90} \cdot xD_2O$ proton conductor.[47] Motivated by these high displacement parameters, other less symmetric space groups were tested to solve these refinement difficulties and therefore, a structural model in suitable subgroups of $R\bar{3}c$ using ISODISTORT were generated. The detailed procedure regarding alternative space groups is described in the supporting information. As we could not find definitive evidence for an assignment away from $R\bar{3}c$, all following Rietveld refinements are performed in the $R\bar{3}c$ space group. To assess the proton substructure in $ZrH_5(PO_4)_3$ the Fourier difference nuclear density maps were constructed (Figure 1a and Figure S6) showing excess (negative) nuclear density where the protons are expected to be accommodated within the structure. Placing protons on these positions examined by the Fourier difference nuclear

density map in the Rietveld refinement gives the best statistical fit and considered final structural model of $ZrH_5(PO_4)_3$ of the analyses herein. When increasing the temperature from 10 K to 100 K, the proton substructure does not change significantly, and the occupancies as well as the atomic positions of each ion in the model are almost constant with only the atomic displacement parameters increasing slightly.

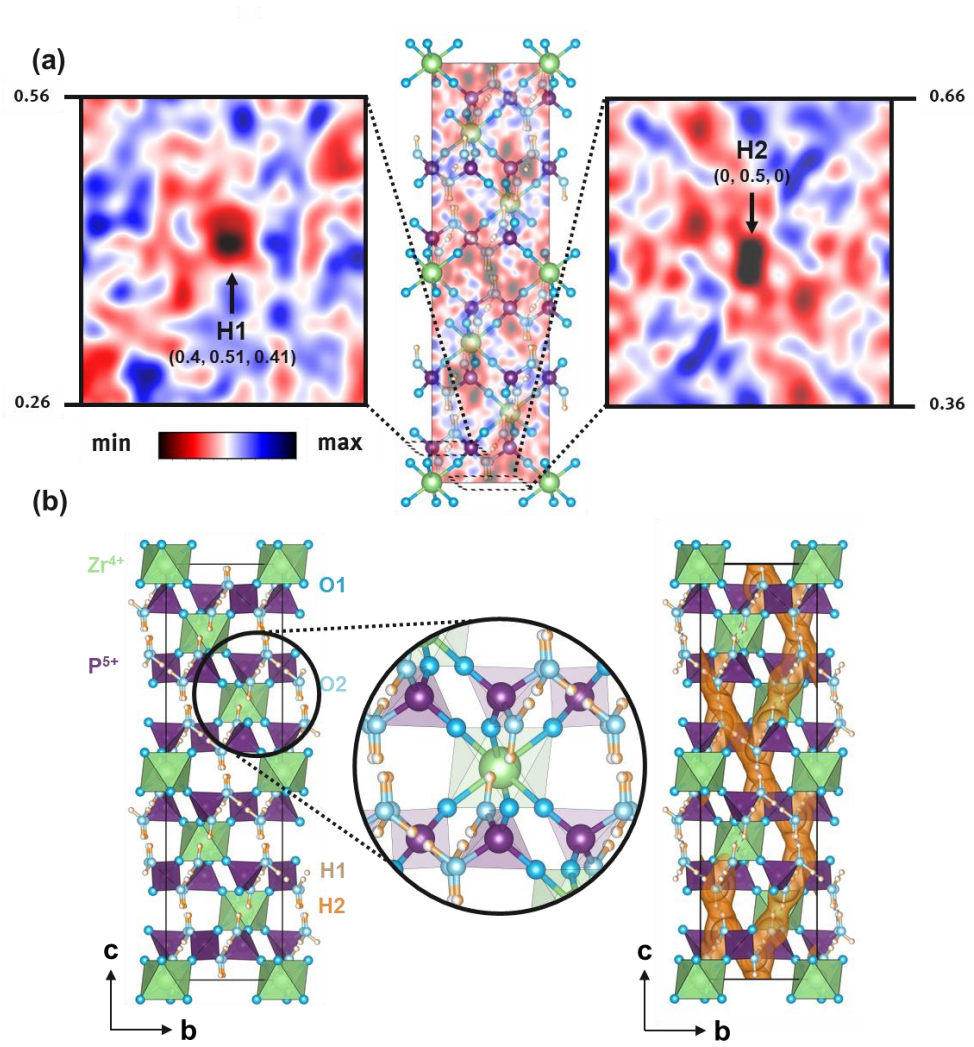

Figure 1: (a) Observed difference Fourier density maps (at 10 K) of the crystal structure using the $R\bar{3}c$ structure model to show the two different regions with negative scattering cross section which indicate the position of the two proton sites. The H1 is shown in the (100)-plane with a distance of the origin of 2.86105 Å and the section is chosen from 0.26 to 0.56 in the z-direction. The H2 is shown in the (100)-plane with a distance of the origin of 0 Å and the section is chosen from 0.36 to 0.66 in the z-direction. (b) Visualization of the structural model in the space group $R\bar{3}c$ on the left side, including the two proton sites determined via the difference Fourier density maps. On the right side, the conduction pathways within the structural model $R\bar{3}c$ are

represented in orange. Although these are 1D conduction pathways, they are linked to each other in 3D.

Structure of $ScH_6(PO_4)_3$. Based on previous literature single-crystal and powder X-ray diffraction analyses, the structurally related scandium analogue, $ScH_6(PO_4)_3$ (or $Sc(H_2PO_4)_3$), crystallizes in either the $R\bar{3}c$[48] or $R3c$[27,28] space groups at room temperature.

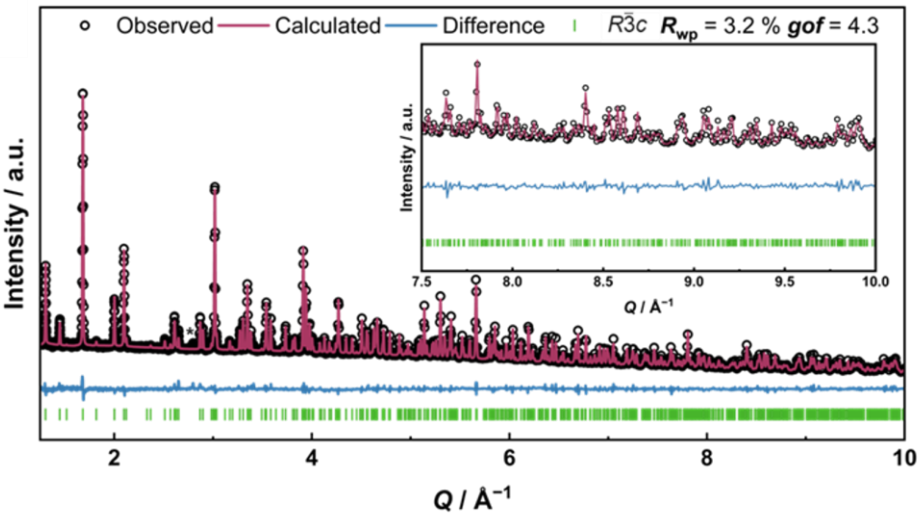

*Figure 2: Rietveld refinement from $ScH_6(PO_4)_3$ against neutron diffraction collected at 10 K using the $R\bar{3}c$ structural model. An unidentified side phase is marked as *.*

The two proposed space groups[27,28,48,49] of $ScH_6(PO_4)_3$ can be differentiated by the loss of inversion symmetry in $R3c$ with respect $R\bar{3}c$.[50] Accordingly, the latter would not generate a bulk SHG signal, whereas $R3c$ does. In fact, results from SHG spectroscopy showed that $ScH_6(PO_4)_3$ exhibits small SHG signals (Figure S3). Although the intensity is five to ten times higher than the signal of $ZrH_5(PO_4)_3$, comparison with the reference materials without inversion symmetry, reveals that the SHG intensity of $ScH_6(PO_4)_3$ is orders of magnitude smaller. We take this as evidence for $ScH_6(PO_4)_3$ being centrosymmetric at least on length scales larger than the coherence length. Based on this consideration, it seems plausible that $ScH_6(PO_4)_3$ crystallizes in $R\bar{3}c$. By using the NPD data, we were able to determine the positions of the H^+ within $ScH_6(PO_4)_3$ (Figure S7 and Tables S6-S8) and the Rietveld refinement of $ScH_6(PO_4)_3$ in $R\bar{3}c$ resulted in satisfactory visual fits and quality indicators (Figure 2) and displacement parameters of the protons and $(PO_4)^{3-}$ in a physically reasonable range. Thus, high displacement parameters such as in $ZrH_5(PO_4)_3$ did not arise for $ScH_6(PO_4)_3$ in $R\bar{3}c$. In Table S9, the O-H bond lengths are summarized. Comparing these bond lengths of $ScH_6(PO_4)_3$ to the values of

$ZrH_5(PO_4)_3$, it is apparent that shorter bonds are observed in $ScH_6(PO_4)_3$. Accordingly, this supports the statement that the protons in $ScH_6(PO_4)_3$ are more localized.

Structural evolution in $Zr_{1-x}Sc_xH_{5+x}(PO_4)_3$. To study the structural evolution and conductivity changes across the slightly Sc-substituted substitution series between $ZrH_5(PO_4)_3$ and $ScH_6(PO_4)_3$, the nominal $Zr_{1-x}Sc_xH_{5+x}(PO_4)_3$ ($0.00 \leq x_{nom} \leq 1.00$; in 0.25 steps) compositional series was targeted by mixing $ZrCl_4$ and $ScCl_3$ in stoichiometric amounts before adding them to the melted H_3PO_4. From the Rietveld refinements of their X-ray diffraction patterns, it was observed that all the targeted materials showed the formation of a $ZrH_5(PO_4)_3$-type phase (Figure S8) and crystallize in the $R\bar{3}c$ space group. To confirm this, the SHG response of each material synthesized was measured, and all showed the same SHG non-activity as $ZrH_5(PO_4)_3$ (Figure S3). As such, all the mixed cation samples are also centrosymmetric, which supports the assignment of space group $R\bar{3}c$. Using Rietveld refinements, the Sc^{3+} content on the metal sites was refined to determine the actual value of x (as x_{ref}), as well as the proton stoichiometry from charge balance. By comparing the refined value of x_{ref} to that of the nominal compositions, it can be observed that all the targeted materials between the two end members (x_{nom} = 0.25, 0.50, 0.75) were Sc^{3+} and therefore H^+ deficient with respect to the targeted compositions (Figure 3a). A reason for that could be different kinetics of the reaction of the two metal centers as – from observation during synthesis – the $ScH_6(PO_4)_3$ precipitates much slower out of solution during the synthesis in comparison to $ZrH_5(PO_4)_3$. The substitution with a nominal Sc^{3+} content of $x_{nom}(Sc) = 0.25$ results in a successful incorporation of a refined Sc^{3+} content of $x_{ref}(Sc) = 0.08(1)$ ($Zr_{0.92}Sc_{0.08}H_{5.07}(PO_4)_3$) in the structure. A nominal Sc^{3+} content

of x_{nom}(Sc) = 0.50 and 0.75 results in the successful incorporation of a refined Sc^{3+} content of x_{ref}(Sc) = 0.14(1) and 0.49(1), respectively.

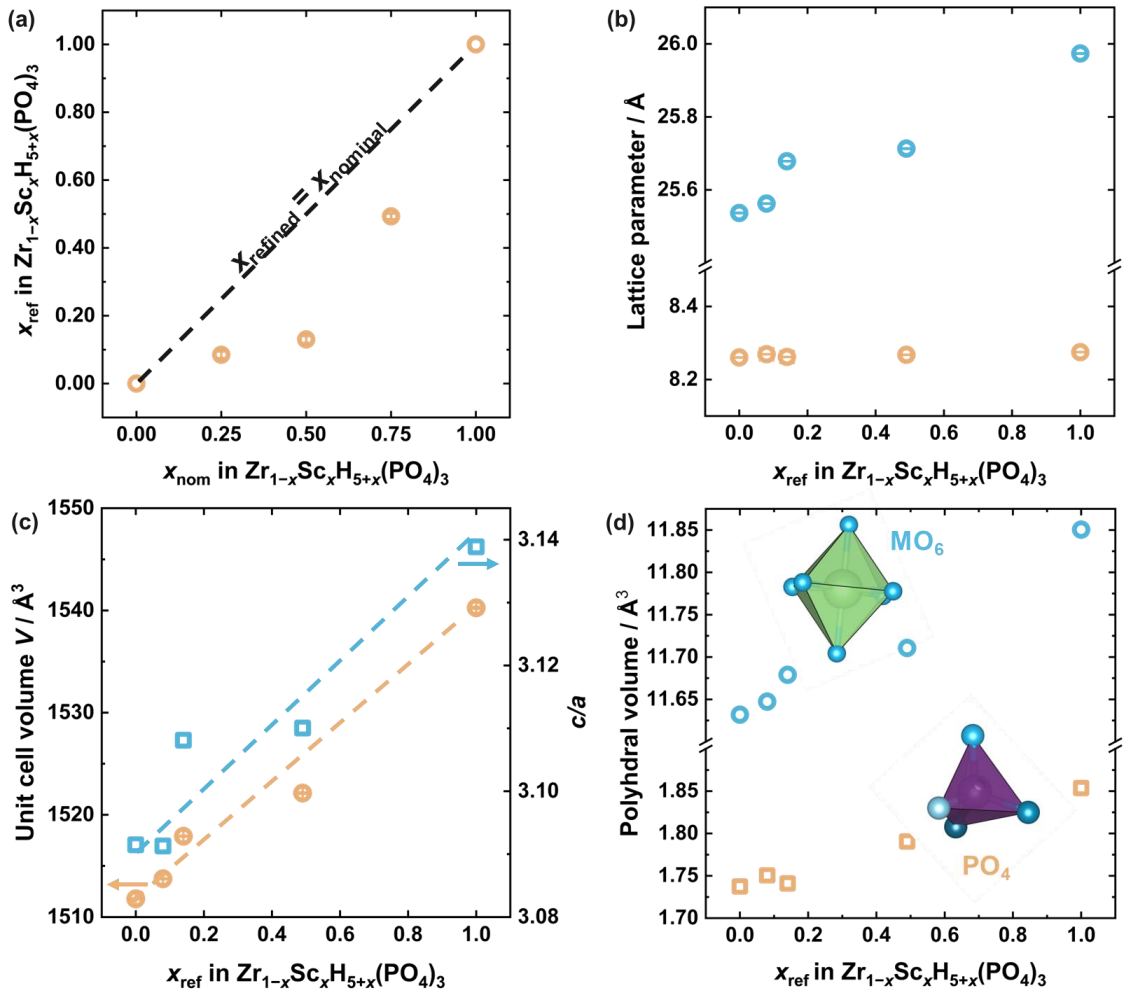

Figure 3: (a) Refined (x_{ref}) against nominal (x_{nom}) Sc^{3+} content in $Zr_{1-x}Sc_xH_{5+x}(PO_4)_3$. The dashed line represents the expected trend for a full Sc^{3+} substitution. (c, b) Lattice parameter and unit cell volume change with the incorporation of Sc^{3+} into $Zr_{1-x}Sc_xH_{5+x}(PO_4)_3$. (d) Change in polyhedral volume of the octahedra and the tetrahedra $(PO_4)^{3-}$ within the substitution series $Zr_{1-x}Sc_xH_{5+x}(PO_4)_3$.

Due to the large discrepancy, all extracted structural parameters are considered with reference to the refined composition, rather than the nominal ($x_{ref} = x$). While the *a* lattice parameter remains almost unchanged, the *c* lattice parameter increases upon Sc^{3+} incorporation. This becomes more obvious in the *c*/*a* ratio and overall results in a linear expansion of the unit cell as the value of *x* is increased (Figure 3b). This may be expected from the larger ionic radius of Sc^{3+} (0.745 Å) compared to Zr^{4+} (0.72 Å), while additional protons are also incorporated into the structure upon substitution.[51] The investigation of the polyhedral volumes reveals that the

MO_6 octahedra become slightly larger with the incorporation of Sc^{3+} (Figure 4c). Similarly, the volume of the $(PO_4)^{3-}$ tetrahedra also increases with higher Sc^{3+} and H^+ contents (Figure 4d).

To further gain insight into this local coordination environments and their evolution ^{45}Sc NMR and ^{31}P MAS NMR spectra were recorded. In the ^{45}Sc NMR spectra (Figure 4a), a single ^{45}Sc resonance from the central transition is observed at approximately −38 ppm for all Zr, Sc mixed samples with a small increase in $\delta(^{45}Sc)$ detected as the Sc^{3+} content increases. The $ScH_6(PO_4)_3$ (x = 1) sample has a different $\delta(^{45}Sc)$ compared to the rest of the sample series at around −15 ppm. A single resonance represents one M position seen across different materials, which is in good agreement with the space group $R\bar{3}c$. Additionally, with mixed Sc, Zr phases (x_{ref} = 0.08, 0.14, and 0.49) the peak is also broadened compared to $ScH_6(PO_4)_3$. This might be due to the longer-range averaging of different Zr^{4+} vs. Sc^{3+} environments.

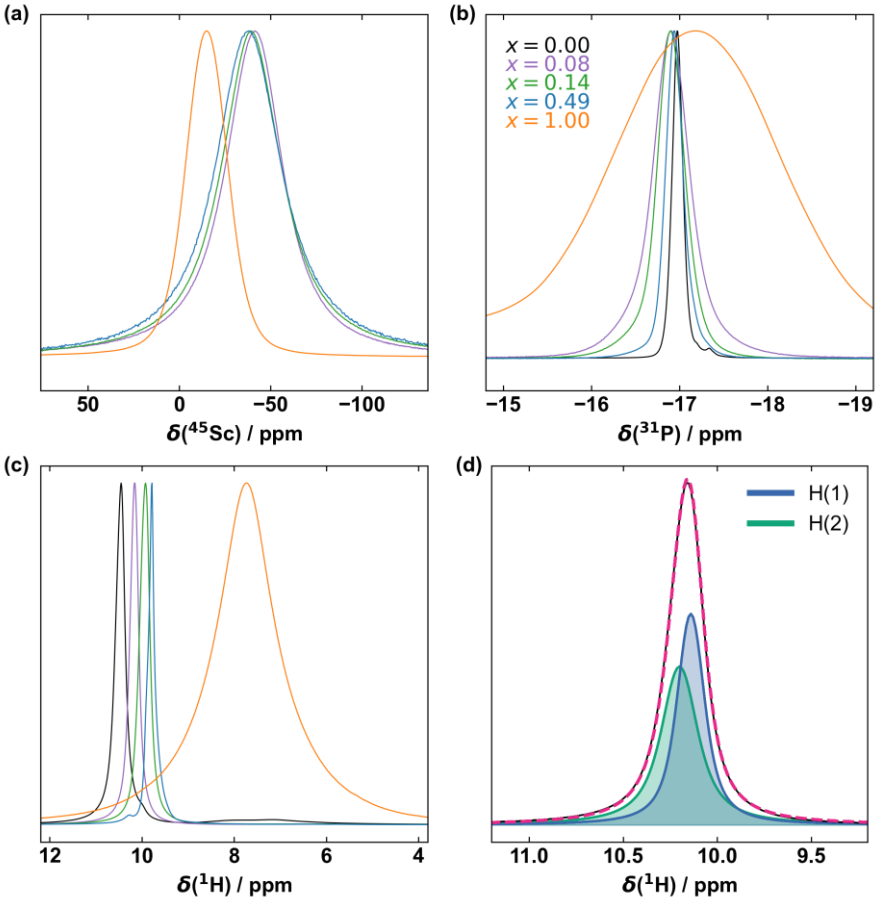

Figure 4: (a) Normalized ^{45}Sc NMR spectra recorded at 7.05 T, (b) ^{31}P MAS NMR spectra recorded at 11.75 T with a MAS frequency of 25.0 kHz, of the Sc-doped $Zr_{1-x}Sc_xH_{5+x}(PO_4)_3$. ^1H MAS NMR spectra of (c) $Zr_{1-x}Sc_xH_{5+x}(PO_4)_3$ sample series recorded at 11.75 T with a MAS frequency of 25.0 kHz. (d) Normalized ^1H MAS NMR spectrum for the x_{ref} = 0.08 sample with deconvolution showing the partially overlapping ^1H signals.

Focusing on the ^{31}P MAS NMR spectra of the Zr containing samples (x_{ref} = 0, 0.08, 0.14, and 0.49) most of the signal is present in a single resonance near the maximum intensity ^{31}P shifts $\delta(^{31}P) \approx -17$ ppm (Figure 4a). An additional peak with relatively very low intensity can be observed at lower $\delta(^{31}P) \approx -8$ ppm, which is assigned to an impurity (Figure S9). However, $ScH_6(PO_4)_3$ again exhibits significantly different behavior than zirconium containing samples (x_{ref} = 0, 0.08, 0.14, and 0.49). The ^{31}P signal is much broader and, shifted toward lower $\delta(^{31}P)$ values. This would indicate a slightly different ^{31}P environment in $ScH_6(PO_4)_3$. One distinctive factor might be the more localized protons, evident in the transport investigated in the next section, influencing the $(PO_4)^{3-}$ tetrahedra, or more precisely the P–O bonds. This might also explain both the signal broadening, because of reduced averaging from limited proton mobility, and change in chemical shift, due to different P–O distances.

The proton localization is also in line with the observations from ^{1}H MAS NMR spectra recorded as a function of Sc^{3+} content (Figure 4c and d). For all zirconium containing samples, the majority of the ^{1}H signal appears at a shift $\delta(^1H)$ of approximately 10.5 ppm, where two (or three in case of x_{ref} = 0.49) overlapping signals can be resolved (Figure 4d and Figure S10-S11). The ^{1}H chemical shifts and relative intensities are summarized in Table S10. The structural model in $R\bar{3}c$ is described by two crystallographically distinct H^+ positions, which is in line with the detected signals. Those two signals monotonically shift to lower $\delta(^1H)$ values as the Sc^{3+} content increases. An additional ^{1}H signal at lower $\delta(^1H)$ is observed in $Zr_{0.51}Sc_{0.49}H_{5.49}(PO_4)_3$ (x_{ref} = 0.49). It is important to note, that despite this, the relative intensity of the H(1) signal (Figure 5d; marked in blue) remains around 50% relative intensity for all samples. This further suggests that the number of ^{1}H signals is influenced by proton dynamics, resulting in additional signal (split from H(2) to H(2) and H(3)) in x_{ref} = 0.49 sample with slower dynamics. Like the other measured nuclei, ^{31}P and ^{45}Sc, the ^{1}H MAS NMR spectrum of $ScH_6(PO_4)_3$ differs significantly from that collected for the other samples. Different average proton environments affect $\delta(^1H)$, while reduced dynamics affect the linewidth.[45] As shown below $ScH_6(PO_4)_3$ is a poor proton conductor, leading to stronger through-space ^{1}H-^{1}H dipolar couplings and, hence, increased ^{1}H linewidth. Thus, different average proton environments affect the $\delta(^1H)$, while reduced dynamics affect the linewidth.

Proton transport in $Zr_{1-x}Sc_xH_{5+x}(PO_4)_3$. The corroborated differences in structural properties particularly linked to the rigidity of the proton substructure, may also be expressed in the proton transport properties. While $ZrH_5(PO_4)_3$ was shown to be an excellent room-temperature, dry-atmosphere proton conductor, neither proton transport in $ScH_6(PO_4)_3$ nor the effect of Sc^{3+}

substitution onto the proton transport in $Zr_{1-x}Sc_xH_{5+x}(PO_4)_3$, has been studied before to the best of our knowledge. Therefore, a combination of bond valence sum calculations, electrochemical impedance spectroscopy and nuclear magnetic resonance analyses is used to analyze the proton transport in $Zr_{1-x}Sc_xH_{5+x}(PO_4)_3$. First, to identify the most likely diffusion pathways in $ZrH_5(PO_4)_3$ and $ScH_6(PO_4)_3$, a bond valence sum approach was used (Figure S12 and Figure S13). In $ZrH_5(PO_4)_3$ and $ScH_6(PO_4)_3$, a singular one-dimensional conduction pathway was found, respectively. However, overall, the H^+ ion-migrations pathways, in both, $ZrH_5(PO_4)_3$ and $ScH_6(PO_4)_3$, appear to be very similar. The H^+ pathways in this system then consists of interpenetrating one-dimensional channels forming a three-dimensional H^+ migration network irrespective of the slightly different structural models in accordance with prior analysis.[13]

Subsequently, temperature-dependent electrochemical impedance spectroscopy was performed to determine the ionic conductivity and resulting activation energy. In all recorded impedance spectra, a single high frequency process (Z_{total}) was observed attributed to proton transport. Additionally, a capacitive low-frequency process is attributed to the blocking behavior of the platinum contacts. The obtained spectra were fit with a parallel resistor-constant phase element in series with a constant phase element (inset Figure 5a). As previously attributed[13], the transport process may be associated with combined bulk and grain boundary contributions to proton conductivity of the material based on the capacitances in the pF range and non-ideal alpha values of 0.91 to 0.97.[52] As a consequence, the following values are considered to be total ionic conductivities. In all samples of $Zr_{1-x}Sc_xH_{5+x}(PO_4)_3$, Arrhenius behavior was observed in the temperature range investigated, with $\ln(\sigma T)$ exhibiting linear dependence on the inverse temperature. This allows the determination of a single macroscopic activation energy (E_a EIS) for total proton conductivity in the investigated temperature range between 20 °C and 80 °C. As the conductivity reduces upon substitution with scandium, the activation energy increases. Accordingly, the non-substituted sample has the highest conductivity of 1.7(4) mS cm^{-1} at room temperature slightly lower than the ca. 5 mS cm^{-1} reported prior.[13] With Sc^{3+} introduction up to $Zr_{0.86}Sc_{0.14}H_{5.14}(PO_4)_3$ proton conductivities above 1 mS cm^{-1} are retained, which then decrease more substantially with x_{ref} down to $3.1 \cdot 10^{-4}$ mS cm^{-1} in $ScH_6(PO_4)_3$. The activation energies indicate an almost linear increase where $ZrH_5(PO_4)_3$ has the lowest activation energy of 0.24 eV while $ScH_6(PO_4)_3$ has the highest value of 0.53 eV within the substitution series.

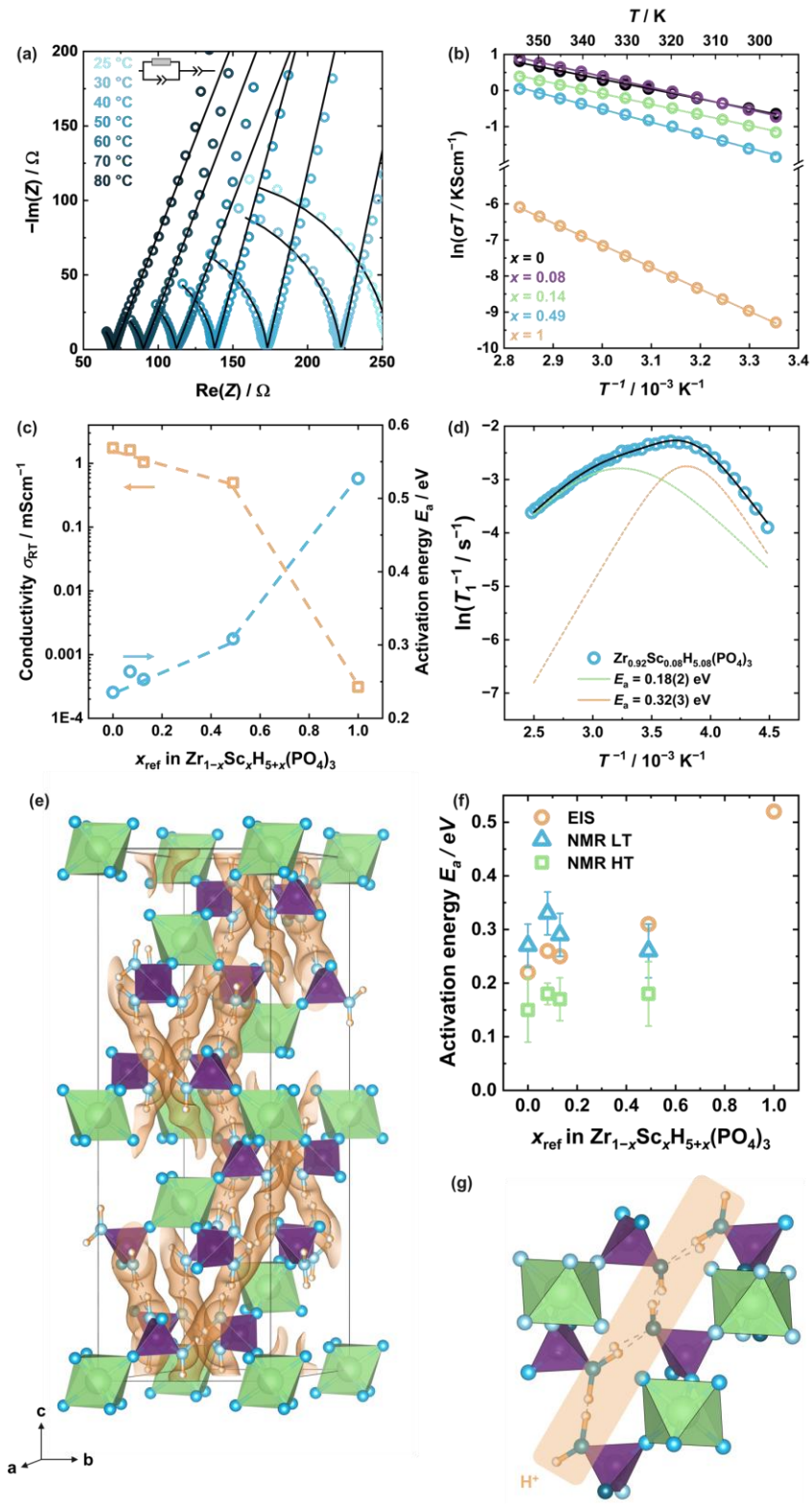

Figure 5: (a) Exemplary Nyquist plots of the $ZrH_5(PO_4)_3$ in the temperature range from RT to 80 °C. (b) All samples follow the linear Arrhenius behavior over the measured temperature range of RT to 80 °C. (c) The conductivity at room temperature σ_{RT} decreases and the activation energy E_a increases with the incorporation of Sc^{3+} into the structure. The dashed lines are guides-to-the-eye. (d) Exemplary Arrhenius plot of the temperature-dependent ^1H relaxation

rates ($1/T_1$) for $Zr_{0.92}Sc_{0.08}H_{5.08}(PO_4)_3$ recorded at Larmor frequency of ν_H = 19.95 MHz, showing two distinct dynamic processes with different activation energies. (e) Interpenetrating one-dimensional H^+ conduction channels forming a three-dimensional H^+ migration network in $Zr_{1-x}Sc_xH_{5+x}(PO_4)_3$ calculated from bond valence calculations. (f) Activation energies extracted from temperature-dependent ^1H NMR (Larmor frequency of ν_H = 19.95 MHz) and electrochemical impedance measurements. (g) Zoom-in onto a 1D proton conduction pathway.

Similar values for the activation energies as those obtained from the EIS measurements were achieved by static variable temperature (VT) ^{1}H NMR experiments in temperature range between 214 and 400 K. ^{1}H saturation recovery at two different proton Larmor frequencies: ν_H = 200.10 MHz (Figure S14), ν_H = 19.95 MHz (Figure 5d and S15) were measured to determine the temperature-dependent ^{1}H relaxation rates ($1/T_1$) for $Zr_{1-x}Sc_xH_{5+x}(PO_4)_3$ with x_{ref} = 0, 0.08, 0.14, and 0.49. The resulting temperature-dependent ^{1}H relaxation rates were analyzed using the modified Bloembergen−Purcell−Pound (BPP) model, which establishes a correlation between NMR relaxation rates and local ionic jump frequencies. Within this model, the relaxation rate attains its maximum value when the H^+ jump frequency aligns with the Larmor frequency of the employed static magnetic field, thereby enabling the determination of activation energies (E_A) and jump rates. Table S11 summarizes the activation energies obtained for the two different Larmor frequencies. A comparison of the Arrhenius plots for these (Figure 5d, Figure S14 and S15) reveal that the higher magnetic field (200.10 MHz) only captures a single dynamic process associated with a higher jump frequency, whereas the lower magnetic field (19.95 MHz) gives evidence for two distinct dynamic processes with lower jump frequencies and different activation energies. From BPP analysis of the Arrhenius plots for both Larmor frequencies, Table S11, a dynamic process with an E_a (19.95 MHz, high-temperature (HT) process; 200.10 MHz) between 0.15 eV and 0.20 eV is visible in all samples. The second process with an E_a (19.95 MHz, low-temperature (LT) process) between 0.26 eV and 0.34 eV is present only in the low MHz dynamical region. The process with a lower activation energy of 0.15 eV to 0.20 eV is relatable to the results obtained from the bond valence sum approach in $ZrH_5(PO_4)_3$, where two 1D H^+ pathways were obtained practically indistinguishable due to their similarity. Additionally, the predicted tendency of lower activation energy in $ScH_6(PO_4)_3$ compared to $ZrH_5(PO_4)_3$ from BVSE calculations does not hold as observed in the experimental activation energies E_a obtained from different methods depicted in Figure 5f. The fact that the BVSE calculations show the opposite trend in the activation energies of $ZrH_5(PO_4)_3$ and $ScH_6(PO_4)_3$ could be because the calculations assume a static, ordered structure and do not consider dynamic disorder, proton-proton correlations, or larger defect formation enthalpies,

considering the shorter O – H bonds in $ScH_6(PO_4)_3$, without any information on the diffusion meachanism.

In summary, the activation energy extracted from EIS measurements increases along with the decrease in ionic conductivity as a function of Sc^{3+} content. This indicates that a higher number of charge carriers in this case does not lead to enhanced ionic transport. In the Sc-substituted samples, it could therefore be the case that a proton cannot jump to the next position because another proton is already bound to the oxygen there, and the protons thus block each other in accordance to the average environment inferred from MAS NMR analysis. Local jump processes were probed via NMR and remain largely unaffected as a function of Sc^{3+} content. Structural analysis suggests a very disordered H^+ substructure in $ZrH_5(PO_4)_3$ describing the H^+ mobility while the partial H^+ localization found in the Sc^{3+} analogue, which may also be explained as a filling of proton vacancies. The structural analysis implies that $ScH_6(PO_4)_3$ is characterized by half-filled proton sites. In such cases, ordered arrangements of vacancies and cations frequently occur in order to mitigate the electrostatic repulsion between neighboring cations. This is also observed in $FeH_6(PO_4)_3$, for instance.[50] This explains the strong drop in the ionic conductivity eventually, where the prior gradual decrease in ionic conductivity upon Sc^{3+} substitution may instead arise from local H^+ ordering close to the incorporated Sc^{3+} centers. tt is basically an intrinsically stabilized vacant structure with the upper section described structural arrangements that makes the high proton conductivity. Compared to other phosphate-based conductors, the distances between the proton and the neighboring PO_4^{3-} tetrahedra in $ZrH_5(PO_4)_3$ are very similar, suggesting that the proton is energetically similar whether it is bound to each of the two tetrahedra.

4. Conclusion

In this work, structural analysis of $ZrH_5(PO_4)_3$ and $ScH_6(PO_4)_3$ was performed, determining the H^+ substructure including positions and occupancies. Studying the proton transport in the slightly Sc-substituted $Zr_{1-x}Sc_xH_{5+x}(PO_4)_3$ with limited Sc incorporation shows that despite of the expansion of the unit cell and the higher charge carrier density in $ScH_6(PO_4)_3$ compared to $ZrH_5(PO_4)_3$, a significant decrease in the proton conductivity as well as increase of the activation energy can be found. The higher conductivity in $ZrH_5(PO_4)_3$ can be rationalized by the more disordered H^+ network, whereas in $ScH_6(PO_4)_3$ the larger number of protons become more localized, resulting in lower proton conductivity.

Supporting Information

The supporting information includes neutron diffraction data of the samples under different temperatures, the Rietveld refinement, tables of crystallographic information from Rietveld refinement, SHG measurement results, Visualization of the Fourier maps, calculated free energies, ^{31}P MAS NMR data, ^{1}H MAS NMR data and bond valence sum approach data.

Notes

The authors declare no competing financial interest.

Acknowledgements

The authors acknowledge financial support from DFG priority program SPP2370 Nitroconversion. The research was supported by the Deutsche Forschungsgemeinschaft (DFG) under grant number ZE 1010/14-1 and MO 2995/5-1. J.K. is a member of the International Graduate School for Battery Chemistry, Characterization, Analysis, Recycling and Application (BACCARA), which is funded by the Ministry for Culture and Science of North Rhine-Westphalia, Germany. The authors also thank Oak Ridge National Laboratory for the allocation of beam time at POWGEN with the proposal number IPTS-34189.1. The authors acknowledge computational resources provided by the HPC Core Facility and the HRZ of the Justus-Liebig-University Giessen.

References

(1) Kreuer, K.-D. Proton Conductivity: Materials and Applications. *Chem. Mater.* **1996**, *8* (3), 610–641. https://doi.org/10.1021/cm950192a.
(2) van Renssen, S. The Hydrogen Solution? *Nat. Clim. Change* **2020**, *10* (9), 799–801. https://doi.org/10.1038/s41558-020-0891-0.
(3) Elam, C. C.; Padró, C. E. G.; Sandrock, G.; Luzzi, A.; Lindblad, P.; Hagen, E. F. Realizing the Hydrogen Future: The International Energy Agency's Efforts to Advance Hydrogen Energy Technologies. *Int. J. Hydrog. Energy* **2003**, *28* (6), 601–607. https://doi.org/10.1016/S0360-3199(02)00147-7.
(4) Hulvey, Z.; Miller, E. L.; Randolph, K.; Rustagi, N.; Satyapal, S.; Thompson, S. T. US Department of Energy Hydrogen and Fuel Cell Technologies Perspectives. *MRS Bull.* **2020**, *45* (1), 57–64. https://doi.org/DOI:%252010.1557/mrs.2019.312.
(5) Secanell, M.; Wishart, J.; Dobson, P. Computational Design and Optimization of Fuel Cells and Fuel Cell Systems: A Review. *J. Power Sources* **2011**, *196* (8), 3690–3704. https://doi.org/10.1016/j.jpowsour.2010.12.011.
(6) Ogungbemi, E.; Wilberforce, T.; Ijaodola, O.; Thompson, J.; Olabi, A. G. Review of Operating Condition, Design Parameters and Material Properties for Proton Exchange Membrane Fuel Cells. *Int. J. Energy Res.* **2021**, *45* (2), 1227–1245. https://doi.org/10.1002/er.5810.
(7) Phair, J. W.; Badwal, S. P. S. Review of Proton Conductors for Hydrogen Separation. *Ionics* **2006**, *12* (2), 103–115. https://doi.org/10.1007/s11581-006-0016-4.

(8) Song, J.; Han, O. H.; Han, S. Nanometer-Scale Water- and Proton-Diffusion Heterogeneities across Water Channels in Polymer Electrolyte Membranes. *Angew. Chem. Int. Ed.* **2015**, *54* (12), 3615–3620. https://doi.org/10.1002/anie.201408318.
(9) Karimi, M. B.; Mohammadi, F.; Hooshyari, K. Recent Approaches to Improve Nafion Performance for Fuel Cell Applications: A Review. *Int. J. Hydrog. Energy* **2019**, *44* (54), 28919–28938. https://doi.org/10.1016/j.ijhydene.2019.09.096.
(10) Mauritz, K. A.; Moore, R. B. State of Understanding of Nafion. *Chem. Rev.* **2004**, *104* (10), 4535–4586. https://doi.org/10.1021/cr0207123.
(11) Chen, X.; Li, G. Proton Conductive Zr-Based MOFs. *Inorg. Chem. Front.* **2020**, *7* (19), 3765–3784. https://doi.org/10.1039/D0QI00883D.
(12) Chen, J.; An, B.; Chen, Y.; Han, X.; Mei, Q.; He, M.; Cheng, Y.; Vitorica-Yrezabal, I. J.; Natrajan, L. S.; Lee, D.; Ramirez-Cuesta, A. J.; Yang, S.; Schröder, M. Ultra-Fast Proton Conduction and Photocatalytic Water Splitting in a Pillared Metal–Organic Framework. *J. Am. Chem. Soc.* **2023**, *145* (35), 19225–19231. https://doi.org/10.1021/jacs.3c03943.
(13) Fop, S.; Vivani, R.; Masci, S.; Casciola, M.; Donnadio, A. Anhydrous Superprotonic Conductivity in the Zirconium Acid Triphosphate ZrH5(PO4)3**. *Angew. Chem. Int. Ed.* **2023**, *62* (18), e202218421. https://doi.org/10.1002/anie.202218421.
(14) Mowe, P.; Pfeiffer, F.; Maus, O.; Zeier, W. G.; Winter, M.; Neuhaus, K. Relationship between Structure and Room-Temperature Charge Transport in Highly Acceptor-Doped Ceria and Zirconia. *Solid State Ion.* **2025**, *428*, 116955. https://doi.org/10.1016/j.ssi.2025.116955.
(15) Kreuer, K. D. Proton-Conducting Oxides. *Annu. Rev. Mater. Res.* **2003**, *33* (1), 333–359. https://doi.org/10.1146/annurev.matsci.33.022802.091825.
(16) Rashid, N. L. R. M.; Samat, A. A.; Jais, A. A.; Somalu, M. R.; Muchtar, A.; Baharuddin, N. A.; Wan Isahak, W. N. R. Review on Zirconate-Cerate-Based Electrolytes for Proton-Conducting Solid Oxide Fuel Cell. *Ceram. Int.* **2019**, *45* (6), 6605–6615. https://doi.org/10.1016/j.ceramint.2019.01.045.
(17) Iwahara, H.; Esaka, T.; Uchida, H.; Maeda, N. Proton Conduction in Sintered Oxides and Its Application to Steam Electrolysis for Hydrogen Production. *Solid State Ion.* **1981**, *3–4*, 359–363. https://doi.org/10.1016/0167-2738(81)90113-2.
(18) Regalado Vera, C. Y.; Ding, H.; Peterson, D.; Gibbons, W. T.; Zhou, M.; Ding, D. A Mini-Review on Proton Conduction of BaZrO3-Based Perovskite Electrolytes. *J. Phys. Energy* **2021**, *3* (3), 32019. https://doi.org/10.1088/2515-7655/ac12ab.
(19) Wang, L. S.; Patel, S. V.; Truong, E.; Hu, Y.-Y.; Haile, S. M. Phase Behavior and Superprotonic Conductivity in the System (1–x)CsH2PO4 – xH3PO4: Discovery of Off-Stoichiometric α-[Cs1–xHx]H2PO4. *Chem. Mater.* **2022**, *34* (4), 1809–1820. https://doi.org/10.1021/acs.chemmater.1c04061.
(20) Haile, S. M.; Chisholm, C. R. I.; Sasaki, K.; Boysen, D. A.; Uda, T. Solid Acid Proton Conductors: From Laboratory Curiosities to Fuel Cell Electrolytes. *Faraday Discuss.* **2007**, *134* (0), 17–39. https://doi.org/10.1039/B604311A.
(21) Baranov, A. I. Crystals with Disordered Hydrogen-Bond Networks and Superprotonic Conductivity. Review. *Crystallogr. Rep.* **2003**, *48* (6), 1012–1037. https://doi.org/10.1134/1.1627443.
(22) Haile, S. M.; Boysen, D. A.; Chisholm, C. R. I.; Merle, R. B. Solid Acids as Fuel Cell Electrolytes. *Nature* **2001**, *410* (6831), 910–913. https://doi.org/10.1038/35073536.
(23) Haile, S. M.; Liu, H.; Secco, R. A. High-Temperature Behavior of CsH2PO4 under Both Ambient and High Pressure Conditions. *Chem. Mater.* **2003**, *15* (3), 727–736. https://doi.org/10.1021/cm020138b.
(24) Nagao, M.; Kamiya, T.; Heo, P.; Tomita, A.; Hibino, T.; Sano, M. Proton Conduction in In3 + -Doped SnP2O7 at Intermediate Temperatures. *J. Electrochem. Soc.* **2006**, *153* (8), A1604. https://doi.org/10.1149/1.2210669.

(25) Xu, Y.; Wu, X.; Ji, X. The Renaissance of Proton Batteries. *Small Struct.* **2021**, *2* (5), 2000113. https://doi.org/10.1002/sstr.202000113.
(26) Jiao, K.; Xuan, J.; Du, Q.; Bao, Z.; Xie, B.; Wang, B.; Zhao, Y.; Fan, L.; Wang, H.; Hou, Z.; Huo, S.; Brandon, N. P.; Yin, Y.; Guiver, M. D. Designing the next Generation of Proton-Exchange Membrane Fuel Cells. *Nature* **2021**, *595* (7867), 361–369. https://doi.org/10.1038/s41586-021-03482-7.
(27) Mel'nikov, P. P.; Komissarova, L. N.; Romanova, T. S.; Stepanov, A. K. Scandium Phosphates. *Izv Akad Nauk SSSR Neorg MaterUSSR* **1976**, *12* (5).
(28) Smolin, Y. I.; Shepelev, Y. F.; Domanskij, A. I. Mechanism of Polycondensation in the Series of Scandium Phosphates. *Izv Akad Nauk SSSR Neorg MaterUSSR* **1984**, *20* (7).
(29) Huq, A.; Kirkham, M.; Peterson, P. F.; Hodges, J. P.; Whitfield, P. S.; Page, K.; Hugle, T.; Iverson, E. B.; Parizzi, A.; Rennich, G. POWGEN: Rebuild of a Third-Generation Powder Diffractometer at the Spallation Neutron Source. *J. Appl. Crystallogr.* **2019**, *52* (5), 1189–1201. https://doi.org/10.1107/S160057671901121X.
(30) Coelho, A. A. {\it TOPAS} and {\it TOPAS-Academic}: An Optimization Program Integrating Computer Algebra and Crystallographic Objects Written in C++. *J. Appl. Crystallogr.* **2018**, *51* (1), 210–218. https://doi.org/10.1107/S1600576718000183.
(31) Campbell, B. J.; Stokes, H. T.; Tanner, D. E.; Hatch, D. M. {\it ISODISPLACE}: A Web-Based Tool for Exploring Structural Distortions. *J. Appl. Crystallogr.* **2006**, *39* (4), 607–614. https://doi.org/10.1107/S0021889806014075.
(32) Momma, K.; Izumi, F. {\it VESTA3} for Three-Dimensional Visualization of Crystal, Volumetric and Morphology Data. *J. Appl. Crystallogr.* **2011**, *44* (6), 1272–1276. https://doi.org/10.1107/S0021889811038970.
(33) Chen, H.; Wong, L. L.; Adams, S. {\it SoftBV} {--} a Software Tool for Screening the Materials Genome of Inorganic Fast Ion Conductors. *Acta Crystallogr. Sect. B* **2019**, *75* (1), 18–33. https://doi.org/10.1107/S2052520618015718.
(34) Chen, H.; Adams, S. Bond Softness Sensitive Bond-Valence Parameters for Crystal Structure Plausibility Tests. *IUCrJ* **2017**, *4* (5), 614–625. https://doi.org/10.1107/S2052252517010211.
(35) Glikman, D.; Braunschweig, B. Nanoscale Effects on the Surfactant Adsorption and Interface Charging in Hexadecane/Water Emulsions. *ACS Nano* **2021**, *15* (12), 20136–20147. https://doi.org/10.1021/acsnano.1c08038.
(36) Kresse, G.; Furthmüller, J. Efficient Iterative Schemes for Ab Initio Total-Energy Calculations Using a Plane-Wave Basis Set. *Phys. Rev. B* **1996**, *54* (16), 11169–11186. https://doi.org/10.1103/PhysRevB.54.11169.
(37) Kresse, G.; Furthmüller, J. Efficiency of Ab-Initio Total Energy Calculations for Metals and Semiconductors Using a Plane-Wave Basis Set. *Comput. Mater. Sci.* **1996**, *6* (1), 15–50. https://doi.org/10.1016/0927-0256(96)00008-0.
(38) Kresse, G.; Hafner, J. Ab Initio Molecular Dynamics for Liquid Metals. *Phys. Rev. B* **1993**, *47* (1), 558–561. https://doi.org/10.1103/PhysRevB.47.558.
(39) Perdew, J. P.; Burke, K.; Ernzerhof, M. Generalized Gradient Approximation Made Simple. *Phys. Rev. Lett.* **1996**, *77* (18), 3865–3868. https://doi.org/10.1103/PhysRevLett.77.3865.
(40) Grimme, S.; Antony, J.; Ehrlich, S.; Krieg, H. A Consistent and Accurate Ab Initio Parametrization of Density Functional Dispersion Correction (DFT-D) for the 94 Elements H-Pu. *J. Chem. Phys.* **2010**, *132* (15), 154104. https://doi.org/10.1063/1.3382344.
(41) Grimme, S.; Ehrlich, S.; Goerigk, L. Effect of the Damping Function in Dispersion Corrected Density Functional Theory. *J. Comput. Chem.* **2011**, *32* (7), 1456–1465. https://doi.org/10.1002/jcc.21759.

(42) Kresse, G.; Joubert, D. From Ultrasoft Pseudopotentials to the Projector Augmented-Wave Method. *Phys. Rev. B* **1999**, *59* (3), 1758–1775. https://doi.org/10.1103/PhysRevB.59.1758.
(43) Blöchl, P. E. Projector Augmented-Wave Method. *Phys. Rev. B* **1994**, *50* (24), 17953–17979. https://doi.org/10.1103/PhysRevB.50.17953.
(44) Togo, A. First-Principles Phonon Calculations with Phonopy and Phono3py. *J. Phys. Soc. Jpn.* **2022**, *92* (1), 12001. https://doi.org/10.7566/JPSJ.92.012001.
(45) Wankmiller, B.; Hansen, M. R. Observation of Li+ Jumps in Solid Inorganic Electrolytes over a Broad Dynamical Range: A Case Study of the Lithium Phosphidosilicates Li8SiP4 and Li14SiP6. *J. Magn. Reson. Open* **2023**, *14–15*, 100098. https://doi.org/10.1016/j.jmro.2023.100098.
(46) Zhang, Z.; Zou, Z.; Kaup, K.; Xiao, R.; Shi, S.; Avdeev, M.; Hu, Y.-S.; Wang, D.; He, B.; Li, H.; Huang, X.; Nazar, L. F.; Chen, L. Correlated Migration Invokes Higher Na+-Ion Conductivity in NaSICON-Type Solid Electrolytes. *Adv. Energy Mater.* **2019**, *9* (42), 1902373. https://doi.org/10.1002/aenm.201902373.
(47) Azad, A. K.; Irvine, J. T. S. Location of Deuterium Positions in the Proton-Conducting Perovskite BaCe0.4Zr0.4Sc0.2O2.90·xD2O by Neutron Powder Diffraction. *Chem. Mater.* **2009**, *21* (2), 215–222. https://doi.org/10.1021/cm8031847.
(48) Boyle, T. J.; Sears, J. M.; Neville, M. L.; Alam, T. M.; Young, V. G. Jr. Structural Properties of the Acidification Products of Scandium Hydroxy Chloride Hydrate. *Inorg. Chem.* **2015**, *54* (24), 11831–11841. https://doi.org/10.1021/acs.inorgchem.5b02030.
(49) Smolin, Yu. I.; Shepelev, Yu. F.; Domanskij, A. I. Determination of Crystal Structure of Monosubstitated Acid Scandium Phosphate, Sc(H2PO4)3. *Kristallografiya 27* (2), 239–241.
(50) Gronych, L. M.; Kraft, M. A.; Hartmann, M.; Faka, V.; Glikman, D.; Koers, I.; Li, C.; Newnham, J.; Braunschweig, B.; Zeier, W. G.; Martinez de Irujo-Labalde, X. Proton Ordering Induces a Polar Structure in the Antiferromagnetic Solid Proton Conductor FeH6(PO4)3. *J. Am. Chem. Soc.* **2025**, *147* (37), 33859–33869. https://doi.org/10.1021/jacs.5c10508.
(51) Shannon, R. D. Revised Effective Ionic Radii and Systematic Studies of Interatomic Distances in Halides and Chalcogenides. *Acta Crystallogr. A* **1976**, *32* (5), 751–767.
(52) Irvine, J. T. S.; Sinclair, D. C.; West, A. R. Electroceramics: Characterization by Impedance Spectroscopy. *Adv. Mater.* **1990**, *2* (3), 132–138. https://doi.org/10.1002/adma.19900020304.

Table of Contents